This is a repository copy of *Discontinuous dewetting dynamics of highly viscous droplets on chemically heterogeneous substrates*.

White Rose Research Online URL for this paper:
https://eprints.whiterose.ac.uk/193414/

Version: Accepted Version

Article:

Discontinuous Dewetting Dynamics of Highly Viscous Droplets on Chemically Heterogeneous Substrates

Jiatong Jiang[1], Frankie Jackson[2], Suparit Tangparitkul[3], Mark C.T. Wilson[2] and David Harbottle[1*]

1. School of Chemical and Process Engineering, University of Leeds, UK

2. School of Mechanical Engineering, University of Leeds, UK

3. Department of Mining and Petroleum Engineering, Chiang Mai University, Thailand

*Corresponding author: David Harbottle, E-mail: D.Harbottle@leeds.ac.uk

Abstract

Hypothesis: Droplet spreading on heterogeneous (chemical/structural) surfaces has revealed local disturbances that affect the advancing contact line. With droplet dewetting being less studied, we hypothesize that a receding droplet can be perturbed by localized heterogeneity which leads to irregular and discontinuous dewetting of the substrate.

Experiments: The sessile drop method was used to study droplet dewetting at a wettability boundary. One-half of a hydrophilic surface was hydrophobically modified with either i) methyloctyldichlorosilane or ii) clustered macromolecules. A Lattice Boltzmann method (LBM) simulation was also developed to determine the effect of contact angle hysteresis and boundary conditions on the droplet dynamics.

Findings: The two surface treatments were optimized to produce comparable water wetting characteristics. With a negative Gibbs free energy on the hydrophilic-half, the oil droplet receded to the hydrophobic-half. On the silanized surface, the droplet was pinned and the resultant droplet shape was a distorted spherical cap, having receded uniformly on the unmodified surface. Modifying the surface with clustered macromolecules, the droplet receded slightly to form a spherical cap. However, droplet recession was non-uniform and daughter droplets formed near the wettability boundary. The LBM simulation revealed that daughter droplets formed when $\theta_R > 164°$, with the final droplet shape accurately described by imposing a diffuse wettability boundary condition.

Keywords: wettability boundary; heterogeneous surfaces; droplet dewetting; daughter droplet generation; highly viscous oil; Lattice Boltzmann method.

1. Introduction

Droplets advancing and receding on surfaces is of great scientific interest because of the many systems where droplet dynamics govern performance, for example in coatings, printing, crop-care, self-cleaning surfaces and oil recovery.[1–4] While droplet dewetting has been extensively studied, few studies have considered the effects of surface heterogeneity on the spontaneous dewetting dynamics of droplets, wherein random chemical and structural variations locally modify the surface energies and subsequently the dynamics of the moving contact line. While less studied, such surfaces are frequently encountered in nature, hence characterizing droplet behavior on heterogeneous surfaces is vital to further our understanding of these complex interfacial problems.

Droplet dynamics on surfaces are of increasing interest[5,6] and through the careful design of the substrate, many studies have shown that droplets can be moved without the need to use an external force, i.e. mechanical or electrical. Two mechanisms are often exploited to move droplets in a particular direction, either i) surface free energy gradients[7–9] or ii) Laplace pressure gradient.[9–11] For the former, the driving force, F_w, to move a droplet from a less wetting surface to a more wetting surface is expressed as: $F_w = \int_{L_l}^{L_m} \gamma(\cos\theta_a - \cos\theta_r)dl$, where dl is the integrating variable from the less wettable region (L_l) to the more wettable region (L_m), γ is the surface tension, and θ_a and θ_r are the advancing and receding contact angles, respectively.[7,12] For the latter, the driving force, $F_{Laplace}$, depends on the geometrical gradient: $F_{Laplace} = -\int_{R_S}^{R_L} S_{TCL} \frac{2\gamma}{(r+R_0)^2} \sin\beta \, dz$, where R_0 and r are the droplet radius and local radius of the wetted geometry, respectively, R_S and R_L are the local radii of the wetted geometry at opposite fronts of the droplet respectively, S_{TCL} is the contact area between the droplet and the wetted geometry and β represents the half apex angle of the wetted geometry.[12,13] Geometrical gradient surfaces are often inspired by nature, for example, the work of Hu et al. mimicked the structural properties of the back of a desert beetle to collect water droplets (fog) using a hybrid surface of hydrophilic nanoneedles embedded within a hydrophobic nanofiber layer.[10] The contrasting wettabilities led the growing droplets (via drop coalescence) to be directed towards the hydrophilic nanoneedles, where the droplet motion was then directed by a reducing radius of curvature. Although the fundamentals of droplet dynamics are understood, droplet behavior is more complex on heterogeneous and non-uniform substrates. Localized differences at the moving contact line become more influential to affect the mobility of a receding droplet.

Carmeliet et al. used the 3D Shan-Chen pseudopotential multiphase Lattice Boltzmann method (LBM) to study the wetting pattern of a droplet on a heterogeneous surface of checkerboard hydrophilic and hydrophobic patches.[14] The equilibrium shape of the droplet was found to depend on the ratio (α) between the patch size and droplet radius. For $\alpha = 0.06$, the droplet shape represented a spherical-cap with a circular contact line, and the apparent contact angle was best described by the Cassie contact angle. With increasing α values, the droplet became increasingly distorted due to the stronger influence of the local wettability, and eventually when $\alpha = 3$, the droplet separated into two daughter droplets with the contact angle best described by the Young's contact angle. On chemically heterogeneous surfaces of equal hydrophilic and hydrophobic patches, the authors proposed a modified Cassie model using the fractions of the actual wetted area to describe the bulk droplet contact angle, highlighting the limitation of the area-based Cassie model.[15]

The effect of local interactions between the solid and liquid droplet were also discussed by Huang who noted the importance of the edge energy of the three-phase contact line (γ_{SLV}), and its variation around the droplet perimeter.[16] For chemical and/or structural heterogeneous surfaces, the heterogeneity becomes increasingly important to the droplet dynamics as it affects the relative contributions of the works of adhesion and cohesion. Variations around the perimeter of a moving droplet have been shown to affect the receding dynamics, resulting in stick-slip motion of the three-phase contact line.[17,18]

Chang et al., studied the mobility of a nanoliter water droplet being dragged over a hydrophilic-superhydrophobic patterned surface.[19] The authors observed preferential wetting on the hydrophilic patches, with small daughter droplets being formed when the droplet was dragged over those patches. The authors attributed the formation of daughter droplets to the pinning force, $F = L\gamma(\cos\theta_r - \cos\theta_a)$ (where L is the pinning width, γ is the water-gas interfacial tension and $\theta_{a/r}$ are the advancing/receding contact angles), with the magnitude of the force dependent on the size of the mother droplet, the interfacial tension and the advancing and receding contact angles.

The unstable motion of a droplet contact line (i.e. pinning and de-pinning) has been observed for evaporating, spreading and receding droplets on heterogeneous surfaces.[20–23] Orejon et al. studied water and ethanol droplets evaporating on substrates of contrasting wettability.[20] While evaporating droplets were observed to recede at a constant rate and with a constant contact angle when deposited on hydrophobic surfaces (i.e. Cytop and polytetrafluoroethylene (PTFE) surfaces), on hydrophilic substrates (i.e. glass and silicon surfaces), the contact line was initially pinned causing the contact

angle to decrease. The extent of contact line pinning was attributed to the intrinsic energy barrier, which is given by the Gibbs free energy as the droplet recedes, $\Delta G = \frac{\gamma \sin^2 \theta_0 (2 + \cos \theta_0)(\delta r)^2}{2r}$, where θ_0 is the equilibrium contact angle and δr is the jump distance of the contact radius.[24,25] For the contact line to de-pin, the apparent contact angle must decrease from equilibrium, thus generating an excess force, $\frac{\partial U}{\partial r} = \partial F = \gamma \sin \theta_0 \delta \theta$ (where γ is the surface tension of water droplet, $\delta \theta$ is the change of apparent contact angle from the equilibrium value), which when $\delta \theta$ is sufficiently large such that $\frac{\partial U}{\partial r} > \Delta G$, the contact line moves/jumps. The extent of contact line pinning was found to correlate to the equilibrium contact angle and surface heterogeneity, with lower θ_0 resulting in longer pinning times, since a larger $\delta \theta$ was needed for $\frac{\partial U}{\partial r}$ to exceed the energy barrier.

The effect of surface patterning on water droplets advancing and receding has been studied by Jiang et al..[26] Using polydimethylsiloxane (PDMS) pillared substrates, the fractional coverage of the pillars was varied from 1.0 (no pillars) to 0.05, and while the apparent advancing contact angle was found to be independent of the fractional coverage, the authors observed a decrease in the apparent receding contact angle with increasing solid fraction, i.e. higher apparent receding contact angle for a more pillared surface. To advance the droplet, the droplet volume was continually increased, and while the liquid-solid contact line remained pinned, the apparent advancement of the droplet on the structured surface was due to the excess liquid volume wetting adjacent pillars, i.e. the contact line did not jump between pillars. When reducing the droplet volume, the droplet contact line on the pillar was initially pinned, but the liquid-gas interface becomes increasingly distorted and eventually leads to the depinning of the liquid-solid contact line. As a function of the structural heterogeneity, the relative contribution of the liquid-solid and liquid-gas contact lines is varied as described by $\Delta A_{act\ SL \leftrightarrows SG}$, and thus modulates the apparent energy required for a droplet to dewet. It is worth noting that the authors observed separation of the water droplet when receding on a pillared surface with a solid fraction of 0.13, although no discussion on the governing mechanism for this separation was provided.

For very high viscosity droplets, Basu and co-workers studied the dewetting dynamics of bitumen on clean hydrophilic glass surfaces.[27,28] When deposited as a thin oil lens, the authors studied the effects of pH and temperature on the dewetting dynamics and equilibrium-wetted states. While no daughter droplets were observed in those studies, when the authors varied the shape of the deposited thin oil film, several daughter droplets were formed as a thin-rectangular film receded to form spherical

droplets.[29] While not influenced by the surface energy, the authors attributed the formation of daughter droplets to rim instabilities as described by Brochard-Wyart and Redon.[30]

In the current study, the spontaneous dewetting of highly viscous oil droplets positioned across a wettability boundary is considered. Substrates were modified using either methyloctyldichlorosilane or clustered macromolecules, with the two routes leading to contrasting wettability boundary conditions and surface heterogeneities, as seen from the nano- and macro-scale characterization of the substrates using atomic force microscopy (AFM) and confocal laser scanning microscopy (CLSM). The complement the experiments and to provide a more quantitative insight into the observed droplet behaviors, a Lattice Boltzmann method (LBM) simulation was developed to shed-light on the critical parameters of the heterogenous patches (area and θ_R) that led to daughter droplets being formed as the droplet receded across the wettability boundary.

2. Materials and Methods

A Colombian heavy crude oil was used throughout the study. The oil was received in primary recovery and without chemical additives. Before use the 1 L stock of crude oil was inverted several times to ensure a homogenous distribution of the crude oil components. The crude oil density and viscosity at 60°C were previously measured to be 0.95 g/cm^3 and 0.4 Pa·s,[31] and the interfacial tension of crude oil-Milli-Q water at 60°C is 22.7 mN/m, measured using the pendant drop method. Ultrapure Milli-Q water (Merck Millipore, USA) with a resistivity of 18.2 MΩ·cm was used in all experiments at an unadjusted pH of 5.5 ± 0.5. Toluene (99%, Fisher Scientific), n-heptane (99%, Fisher Scientific) and methyloctyldichlorosilane (98%, Alfa Aesar) were used as received and without further purification.

Substrate preparation: Borosilicate glass slides (> 80% SiO$_2$) of L = 35 mm and W = 25 mm were used as the test substrates. Two methods were used to modify the wettability of one-half of the test substrate, see Fig. S1 of the Supplementary Information which describes in detail each step of the two contamination methods. The first method used methyloctyldichlorosilane to silanize the glass surface, and to avoid modifying the full test substrate, PTFE tape was tightly wrapped around one-half of the glass slide and sealed with aluminum foil. 1 mL of methyloctyldichlorosilane was added to a PTFE weighing boat and placed in a desiccator with 1 glass slide horizontally positioned 10 cm from the PTFE boat. The desiccator was closed for 30 min to allow for vapor deposition of the volatile silane solution. The silane modified test substrates were washed with Milli-Q water and dried with nitrogen gas. The second method involved contaminating one-half of the glass slide in diluted heavy crude oil

which was mixed with heptol 1:1 (heptane:toluene, 1:1 vol:vol) at 5 g/L. 20 mL of the diluted crude oil was poured into a glass beaker and the test substrate was vertically positioned such that one half of the glass slide was submerged in the diluted crude oil. The glass slide was left to soak for 24 h before being washed using heptol 1:1 to remove any loosely bound material and dried in a fumehood for 24 h. Following these methods, those protected surfaces showed low contaminations levels, hence are described as being only partially contaminated, while for the unprotected surfaces, the contamination levels were high, and are described as being fully contaminated, see Table 1 for the complete description of the prepared surfaces. For all prepared surfaces the wettability was measured by depositing a 10 ± 1 µL sessile droplet onto the test substrate in a desired location. All contact angle measurements were repeated in triplicate with the average value reported.

Oil droplet dewetting: All experiments were conducted at $60 \pm 1^{\circ}$C with the temperature chosen based on our previous study where very slow and very fast dewetting dynamics were observed at near ambient temperatures and $\sim 80^{\circ}$C, respectively.[31] Prior to each test all fluids and surfaces were pre-heated for 30 min. A beveled pipette tip (1-200 µL, Fisher Scientific) was attached to the 100 µL auto-pipette of the Theta tensiometer (Biolin Scientific, Finland) and used to deposit a 10 ± 1 μL oil droplet at the boundary between the uncontaminated and contaminated surfaces. The droplet volume was optimized to ensure that gravitational and inertial effects were negligible, and that the full dewetting of the droplet could be imaged by both the side-view and top-view cameras. The droplet was deposited at the wettability boundary and would spread to approximately 8 to 10 mm in diameter (dependent on the test substrate), forming a thin oil film with a contact angle of $\sim 174 \pm 1^{\circ}$ (measured through the air-phase).

A schematic of the experimental set up is shown in Fig. 1. With the oil droplet spread on the test substrate, 60 mL of the pre-heated Milli-Q water was dispensed into the base of the test cell at ~1,400 mL/min. The receding oil droplet was recorded at 2 fps using the side-view (camera 1, Fig. 1) and top-view (camera 2, Fig. 1) cameras. The initial condition ($t_i = 0$ s) was taken to be the first image when the oil film was fully submerged by Milli-Q water. The receding oil droplet was recorded for 2000 s. All experiments were completed at least 3 times and showed very good reproducibility on the silanized-modified surface, with slightly greater variability on the oil-contaminated surfaces, see Fig. S2 of the Supporting Information. Typical values for the dimensionless parameters including the Bond number, Reynolds number, Weber number and Capillary number are provided in Section S3 of the Supporting Information. Those values were calculated based on the receding rate of a heavy crude oil

droplet deposited on an un-modified hydrophilic glass substrate, which had a water contact angle of ~5 ± 1°. As such, the reported values are taken to be maximum values as the rate of droplet recession exceeded that of those measured on the modified substrates.
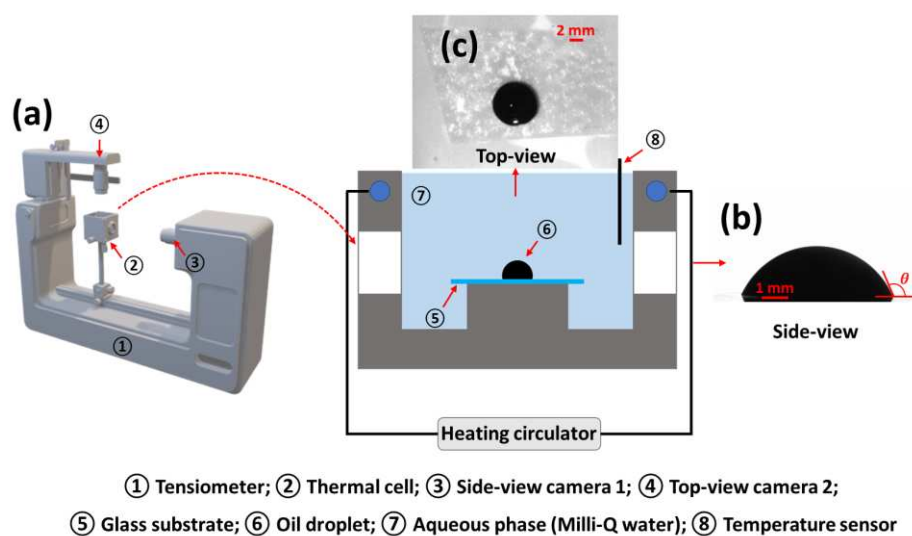

Figure 1. a) Schematic of the measurement cell used to observe oil droplets receding on the test substrates. The test substrate was slightly elevated from the bottom of the measurement cell to better visualize the deposited and receding oil droplet. Typical images collected using the side-view and top-view cameras are shown in (b) and (c), respectively. The temperature of the measurement cell was maintained at 60 ± 1°C using a circulating water bath. It should be noted that all contact angles (θ) are measured through the aqueous phase (b).

Data analysis: Images were processed to measure the three-phase contact angle (θ) and contact line length (Points A and B, Fig. 4) as the oil droplet recedes. For the contact angle, images were processed using the OneAttension software (Biolin Scientific, Finland), and for the silanized surfaces both the left (silanized surface) and right (unsilanized surface) contact angles were measured. For the oil-contaminated surface only the right (unmodified surface) contact angle could be accurately measured, with the droplet dynamics complicating the ability to accurately measure the left contact angle, see further discussion below. An edge-detection code written in MATLAB was used to measure the contact line length. The gray-scaled images were processed to determine the droplet profile based on black/white color thresholding, with each pixel analyzed to identify the contact line and the pixel position from which the contact line length could be measured (pixel/mm).

Topographical imaging: Atomic force microscopy (AFM) and confocal laser scanning microscopy (CLSM) were used to image the test substrates at the micron and millimeter length scales, respectively. Topographical images of 5 μm^2 were obtained using an Innova® AFM (Bruker) operated in tapping mode. A monolithic silicon cantilever (Tap300AI-G, Budget Sensors) with a force constant of ~40 N/m and resonance frequency of 300 kHz was used for the measurements. Multiple locations were imaged and the amplitude set point was 0.6 V. Using the NanoScope software, images were flattened with minimal polynomial order and the root-mean-square roughness (R$_q$) calculated. A Zeiss LSM 800 with a C Epiplan-Apochromat 20/0.7 objective lens and a working distance of 1.3 mm was used to scan an area of size 1.18 mm × 5.65 mm with a z-range of ~1 μm (approximately 100 slices). All image slices were processed using the Zeiss Confomap ST v.7.4 software to reconstruct a 3D image of the test substrate.

3. Simulation Method

To assist in the interpretation of the experimental observations, droplet dewetting simulations were also performed using a multiphase Lattice Boltzmann method code. The LBM is a mesoscopic simulation approach based on the dynamics of discretized particle probability distribution functions. It is an established numerical scheme for multiphase flow simulation that has been validated against experiments and empirical models, and is well suited to capture effects of surface chemistry and topography on wettability.[32–34] An in-house code is used, which implements the same multiphase model as described by Al-Ghaithi et al..[35] The basic concept is to build a simplified kinetic model which connects the essential physics of microscopic/mesoscopic processes so that the macroscopic averaged properties obey the desired macroscopic equation.[36] Molecular velocities in 3D space are represented by a set of 19 discrete velocities defining a lattice structure connecting uniformly spaced nodes. At each node, each discrete velocity $\boldsymbol{e}_\alpha$ has an associated discrete probability density function value f_α that evolves with time t according to the Lattice Boltzmann equation:

$$f_\alpha(\boldsymbol{x} + \boldsymbol{e}_\alpha \delta t, t + \delta t) = f_\alpha(\boldsymbol{x}, t) - \Omega_{\alpha\beta} \left[f_\beta(\boldsymbol{x}, t) - f_\beta^{eq}(\boldsymbol{x}, t) \right]$$

$$+ \delta t \left[S_\alpha(\boldsymbol{x}, t) - \frac{1}{2} \Omega_{\alpha\beta} S_\beta(\boldsymbol{x}, t) \right] \tag{1}$$

where $\boldsymbol{x}$ is the node location, δt is the time step, f_β^{eq} is the equilibrium distribution function, and $\Omega_{\alpha\beta}$ is the multiple-relaxation-time collision operator.[37] Hence, at each time step, distribution function values relax towards a local equilibrium and propagate ('stream') from each node to its near neighbors.

To simulate multiphase flow, the source term S_α is used to incorporate intermolecular forces via the Shan-Chen pseudopotential model[38,39], which introduces local attractive forces given by:

$$F(x,t) = -G\psi(x,t) \sum_\alpha w_\alpha \psi(x + e_\alpha \delta t, t + \delta t) e_\alpha \tag{2}$$

where G is the strength of the phase interaction force, w_α are weights, and

$$\psi(x,t) = \sqrt{6\left(p - \frac{1}{3}\rho(x,t)\right)/G}. \tag{3}$$

The density $\rho(x,t) = \sum_\alpha f_\alpha(x,t)$ and the pressure p is given by the Carnahan-Starling equation of state, modified to control the thickness of the diffuse interface for minimization of spurious velocities.[40,41] The improved multiphase multiple-relaxation-time (MRT) forcing scheme of Li et al. is used.[42]

In the presented simulations, the phase interaction value is set to $G = -1$ for automatic phase separation. No-slip boundaries are modelled with the simple half-way bounce back method. A domain size of $141 \times 55 \times 90$ lattice units[3] is used with the droplet radius of 27 lattice units located in the center of the surface. The densities of the aqueous phase and the droplet are 0.216 and 0.0732 lattice units, respectively, and the dynamic viscosity ratio between the two phases was set at 14.78. The surface wettability is controlled by a geometric contact-angle model with controllable hysteresis properties.[35] The advancing and receding contact angles are defined for oil-wet and water-wet regions in the simulation[43] and the specific parameters are described in the relevant figure captions and associated text in Section 4.

For the simulation mimicking the silanized surface, the substrate was sharply divided into two equal-sized areas at the centre of the substrate ($x = 70$ lattice units) and each surface shows different wettability. For the simulation mimicking the oil-contaminated surface, a diffuse boundary with a width of 14 lattice units is generated at the center of the substrate. The boundary width was selected according to the width of the gradient boundary that was analyzed by CLSM scanning, which is about 25% of the droplet diameter. Across the diffuse boundary, the wettability was given by linearly interpolating between the two surface wettabilities.

To verify that the simulations are independent of the lattice resolution, simulations on the patch-patterned surface were repeated using a doubled lattice resolution (i.e. 54 nodes per droplet radius). The same dynamics and final outcomes were observed, as shown in Fig. S6.

4. Results and Discussion

Prior to studying the droplet receding dynamics on the modified substrates, each substrate was characterized to determine the effect of the contamination method on surface coverage, roughness and wettability. The control substrate was taken to be a clean glass slide which was relatively smooth and featureless with an R_q value of 0.5 nm, as measured by AFM (Fig. 2a, Surface I). The water droplet contact angle (air-water-glass substrate) was ~5 ± 1°, which reflected the strong water-wetting behavior of the untreated, clean glass substrate (Table 1). By modifying one-half of the clean glass substrate with methyloctyldichlorosilane, the water droplet contact angle increased to 89 ± 1° and the R_q value was 7.5 nm, significantly higher than the unmodified surface (Fig. 2c, Surface III). Although PTFE tape and aluminum foil were used to protect the other half of the glass substrate, partial deposition of methyloctyldichlorosilane on the surface could not be avoided. On this surface the water droplet contact angle was 19 ± 1° and the R_q value was 1.5 nm (Fig. 2b, Surface II). The observed nano-scale structures on both surfaces (II and III) were consistent with those seen by Aissaoui et al. who commented that silane agglomerates form via a nucleation and growth mechanism.[44]
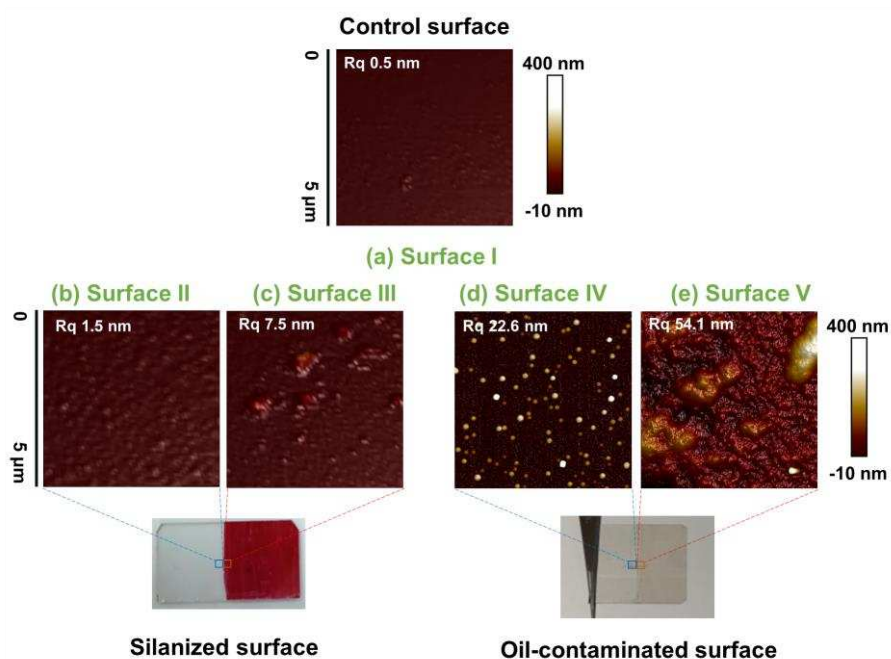

Control surface

Rq 0.5 nm   400 nm

-10 nm

(a) Surface I

(b) Surface II   (c) Surface III   (d) Surface IV   (e) Surface V

Rq 1.5 nm   Rq 7.5 nm   Rq 22.6 nm   Rq 54.1 nm   400 nm

-10 nm

Silanized surface   **Oil-contaminated surface**

Figure 2. AFM tapping mode images of the control substrate – Surface I (a); partially-silanized substrate – Surface II (b); fully-silanized substrate – Surface III (c); partially-oil-contaminated substrate – Surface IV (d); and fully-oil-contaminated substrate – Surface V (e). For the modified substrates, the contact angles were measured at a droplet center distance of ~0.8 cm from the visual wettability boundary.

Table 1. Contact angles of the prepared surfaces.

Test substrate		**Water droplet contact angle (°)[†]**	**Oil droplet contact angle (°)[¥]**
Control	Surface I	5 ± 1	50 ± 1
Partially-silanized	Surface II	19 ± 1	56 ± 3
Fully-silanized	Surface III	89 ± 1	148 ± 2
Partially-oil-contaminated	Surface IV	27 ± 3	64 ± 7
Fully-oil-contaminated	Surface V	94 ± 3	81 ± 6

[†]Contact angle of a water droplet deposited on the substrate in air; [¥]Contact angle of an oil droplet deposited on the substrate and subsequently submerged in the aqueous phase. All contact angles were measured through the aqueous phase.

For surfaces contaminated by the heavy crude oil, the surface deposits were likely to be asphaltenes and naphthenic acids. However, from FTIR analysis (Fig. S3 of the Supporting Information), the deposit was found to be abundantly asphaltenic, which is reasonable since the oil had a very high asphaltenes content, 39.5 wt% as determined by the SARA method.[45] For the half-surface submerged in the diluted heavy crude oil, the water droplet contact angle was $94 \pm 3°$ and the R_q value was 54.1 nm (Fig. 2e, Surface V). For the protected half-surface, the water droplet contact angle was $27 \pm 3°$ and the R_q value was 22.6 nm (Fig. 2d, Surface IV). The higher contact angle and surface roughness relative to the unmodified substrate confirmed the deposition of oil-soluble species beyond the identified wettability boundary. While effort was made to avoid this effect, capillary action of the solvent led to partial contamination of the surface. When imaged using CLSM (Fig. 3), a diffuse-boundary was observed on Surface IV. The dark green regions represent greater surface roughness which is seen to diminish with increasing distance from the visual boundary. Within the resolution of the measurement technique, a diffuse-boundary was clearly observed over ~2.0 mm (Fig. 3b), but few oil deposits (clustered macromolecules) were observed beyond that region, see the higher magnification image in Fig. 3a inset. A similar approach using CLSM was used to measure the

boundary region on the silanized surface but was unsuccessful due to the limiting resolution of the technique and the strong reflection from the glass slide.
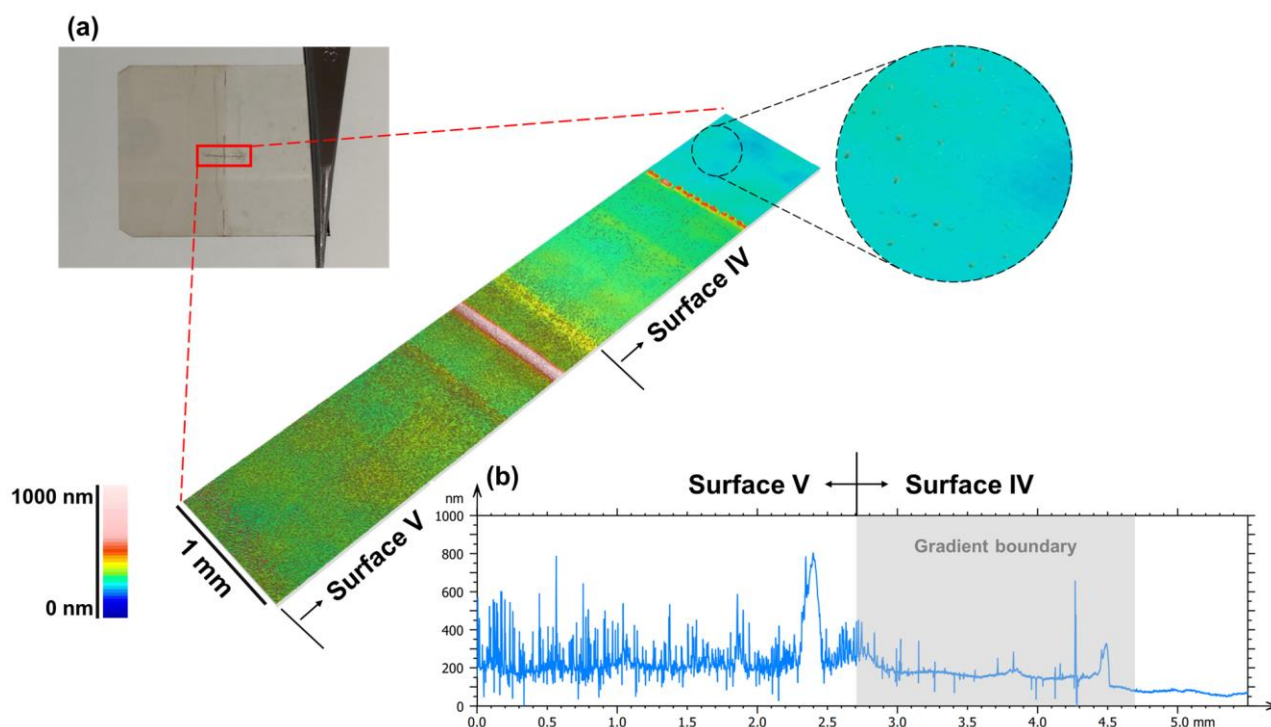

Figure 3. Microscopy images of the half-half oil-contaminated glass substrate. a) Optical microscope image showing the boundary between the oil-contaminated and non-contaminated surfaces. b) High resolution confocal laser scanning microscopy image of the oil-contaminated glass substrate with the imaged region corresponding to the red box in (a). A diffuse boundary of partial oil-contamination on the glass substrate is highlighted by the gray box in the line profile plot (b). The apparent increase in thickness at 2.4 mm (b) is an artifact which resulted from a scratched line underneath the glass slide. This line was used to help position droplets across the wettability boundary.

Oil droplet dewetting on silanized surfaces: The dewetting dynamics of a heavy crude oil droplet deposited at the wettability boundary of Surfaces II and III (partially- and fully-silanized surfaces) are shown in Figs. 4a (top view) and b (side view). Once the added Milli-Q water floods over the deposited oil droplet, the droplet spontaneously dewets. However, with contrasting oil droplet contact angles (Table 1), the oil droplet dewets asymmetrically. By monitoring the dynamic contact line it was seen that contact Point B on Surface III (Fig. 4b and c) remained pinned, while contact Point A on Surface II (Fig. 4b and c) moved towards Surface III. It should be noted that while the silhouette side view appears to show a hemi-spherical cap, the top view reveals the droplet contact line is pinned at the

boundary of Surfaces II and III (Fig. 4a), therefore, the final droplet shape resembled that of a distorted spherical cap.
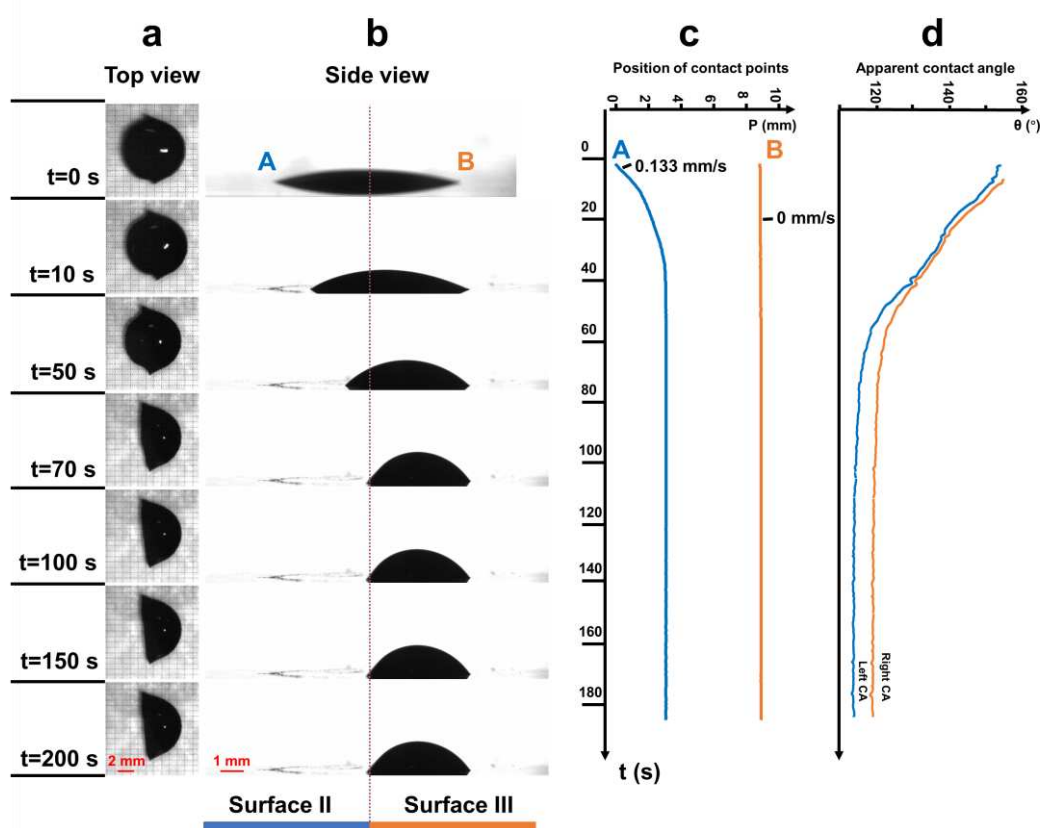

Figure 4. Dynamic dewetting of a heavy crude oil droplet initially positioned centrally at the wettability boundary. The glass substrate was treated with a silanizing agent and Surfaces II and III had water contact angles of $19 \pm 1°$ and $89 \pm 1°$, respectively. Top-view (a) and side-view images (b) of the receding oil droplet with time, $t = 0 - 200$ s. Time-dependency of the droplet contact points A and B (c) and the apparent droplet contact angles (d). In (c), 0 mm is the initial position of contact point A. Repeat measurements on the silanized surfaces showed very good reproducibility for both the receding rates and steady-state apparent contact angles, see Fig. S2a of the Supporting Information.

With the Bond number < 1 the dewetting process is strongly governed by the changing surface energies.[46] For an oil droplet to recede, the solid-water (sw) interface replaces the oil-solid (os) interface, and assuming that $\Delta A_{o/w}$ is negligible, which is reasonable for the case of a droplet receding on a substrate, the energy associated with droplet displacement is given by:[47]

$$\frac{\Delta G}{\Delta A} = \sigma_{SW} - \sigma_{OS} \tag{4}$$

Based on the Young's equation, $\cos \theta = \frac{\sigma_{OS} - \sigma_{SW}}{\sigma_{OW}}$, Eq. 4 can be simplified to:

$$\frac{\Delta G}{\Delta A} = -\sigma_{OW} \cos \theta \tag{5}$$

which shows that the energy change during oil droplet recession is dependent on σ_{OW} and θ. For spontaneous oil droplet recession, $\frac{\Delta G}{\Delta A}$ must be negative. With σ_{OW} being positive, Eq. 5 shows that a droplet can only spontaneously recede if θ is < 90° (measured through the aqueous phase). For the deposited oil droplet on Surface II, $\theta = 56 \pm 3°$ and $\frac{\Delta G}{\Delta A} = -12.7$ mN/m and on Surface III, $\theta = 148 \pm 2°$ and $\frac{\Delta G}{\Delta A} = 19.3$ mN/m. The negative Gibbs free energy change on Surface II confirms the droplet will recede but not on Surface III where the Gibbs free energy change is positive and thus the contact line is pinned. The interpretation of droplet behavior is consistent with that determined from calculating the spreading parameter (S) for the oil droplet receding on all five surfaces (Table 1) in water, see section S3 of the Supporting Information.
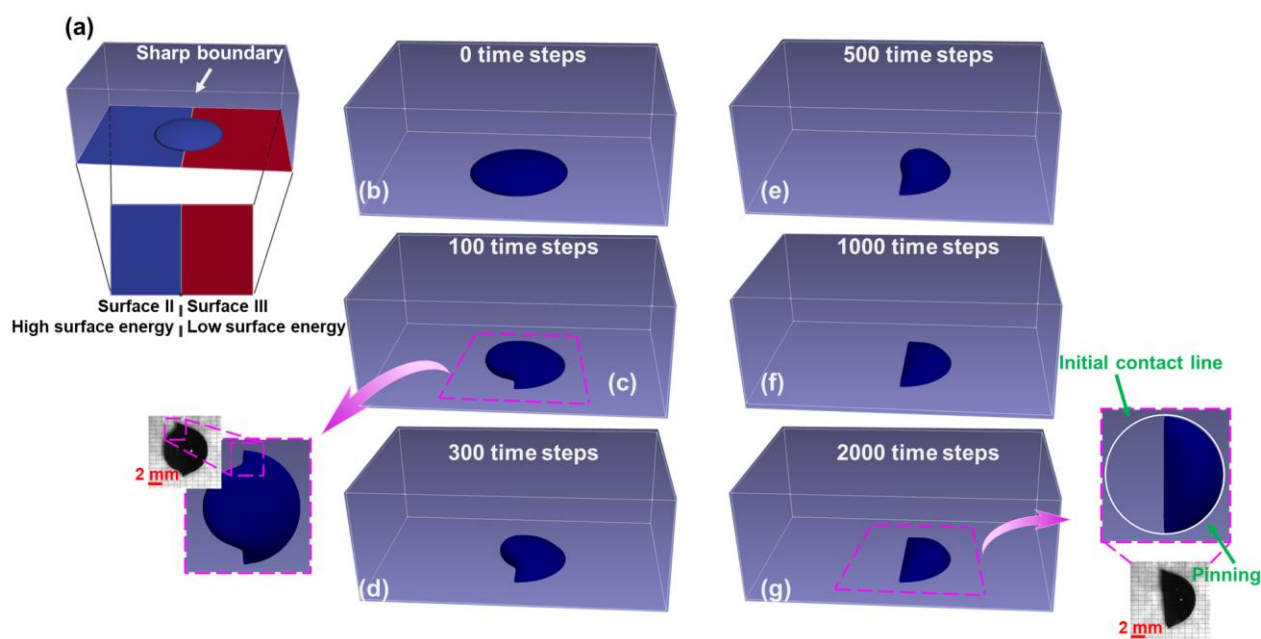

Figure 5. Simulated droplet dewetting using the Lattice Boltzmann method. To mimic the experiment the substrate was formed using a sharp boundary dividing a high surface energy substrate (Surface II), with advancing and receding contact angles through the continuous phase of 56° and 56°, and a low surface energy substrate (Surface III), with advancing and receding contact angles of 140° and 175°, respectively (a). Snap-shots of the receding droplet are shown in b-g of increasing LBM time-steps. The steady-state condition is shown at 2000 time-steps.

The final shape of the oil droplet on Surface III was a distorted spherical cap which formed due to the three-phase contact line on Surface III being pinned as the heavy crude oil droplet recedes on Surface II. As it was not possible to experimentally measure the advancing contact angles (θ_A) for the immersed oil droplets due to the high oil viscosity, the droplet dewetting process was simulated using the Lattice Boltzmann method wherein θ_A and θ_R can be independently adjusted. Figure 5 shows a LBM simulated droplet dewetting process that describes the dynamics and steady-state condition of the experiment (Fig. 4). To establish the LBM parameters, both contact angles (advancing and receding) were initially taken to be the measured steady-state contact angles, see Table 1. However, as the droplet receded from the high surface energy substrate, it was also found that the droplet contact line on the low surface energy substrate advanced (Fig. S4b), which contrasted the pinned contact line seen in the experiment (Point B, Fig. 4b). To avoid the contact line advancing it was necessary to decrease the advancing contact angle (measured through the aqueous phase) relative to the measured steady-state contact angle. Note that the steady-state contact angles in Table 1 were obtained after droplet recession, and therefore cannot be expected to be a good representation of θ_A. For the LBM simulation shown in Fig. 5, the advancing and receding contact angles on the two surfaces were 56° and 56° (mimicking Surface II) and 140° and 175° (mimicking Surface III). The θ_R on Surface III was taken to be 175° based on the measured receding contact angle (Fig. S4c). It is noted that the LBM values may not represent the true θ_A (such values were difficult to measure due to the very high oil viscosity), but highlights the importance of the advancing contact angle, and hence contact angle hysteresis, on the low surface energy substrate in inhibiting the motion of the contact line as the droplet recedes from the high surface energy substrate. When using the adjusted contact angles, the equilibrium shape of the droplet was that of a distorted spherical cap with a straight contact line at the wettability boundary, as seen in the experiments.

Oil droplet dewetting on oil-contaminated surfaces: The dewetting dynamics of heavy crude oil droplets were further studied on glass substrates contaminated by clustered macromolecules. The contamination method was optimized such that the water contact angle on the contaminated surface (Surface V) was approximately equal to that of Surface III, see Table 1. As previously discussed, the contamination method also led to partial contamination of the surface close to the wettability boundary, Surface IV. Based on the oil droplet contact angles on Surfaces IV and V (Table 1), the energy change during droplet recession is −9.99 mN/m and −3.55 mN/m for Surfaces IV and V, and thus the heavy crude oil droplet can recede on both surfaces (see Fig. 6), with droplet recession being easier on Surface IV.
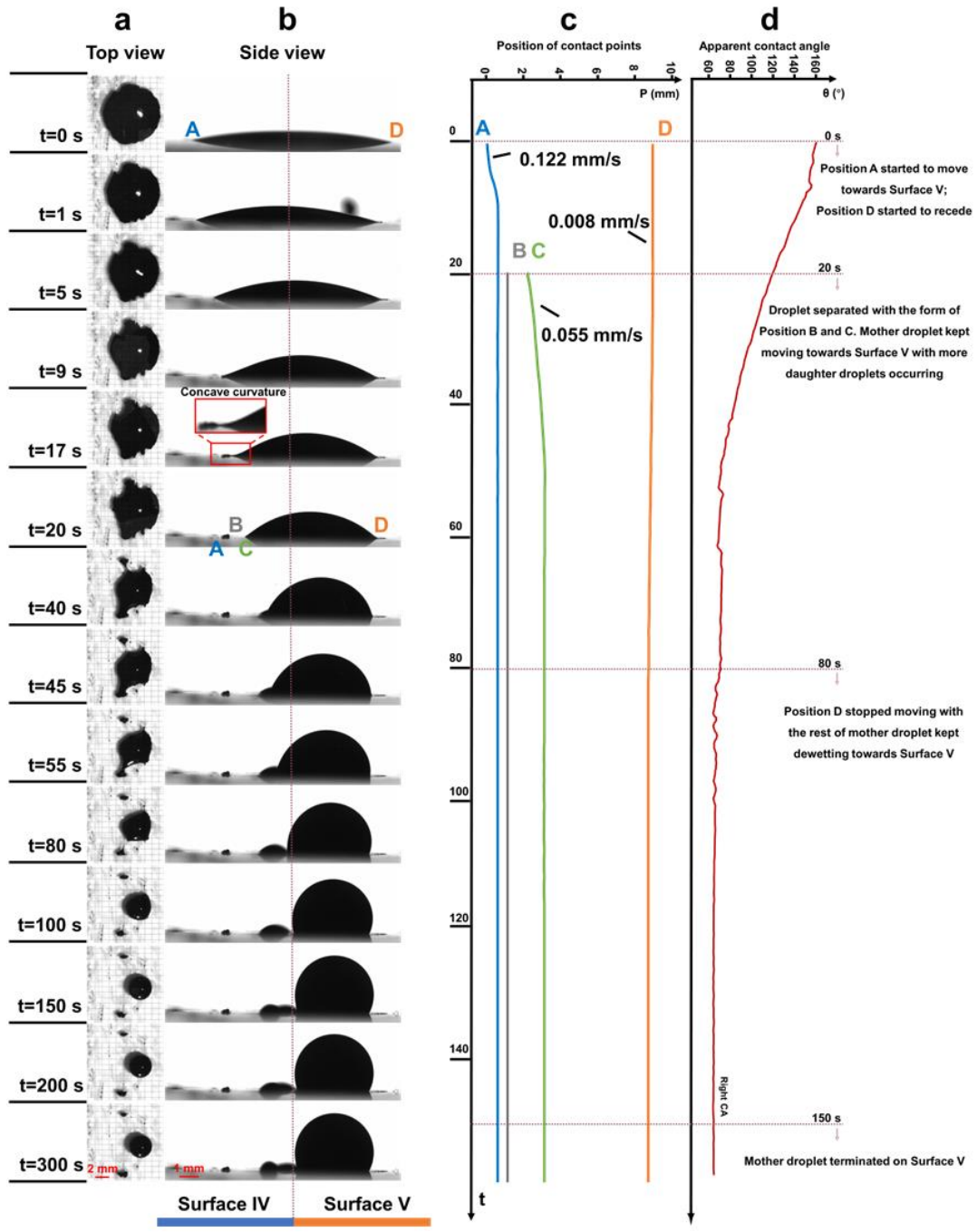
Figure 6. Dynamic dewetting of a heavy crude oil droplet initially positioned centrally at the wettability boundary. The glass substrate was treated with a solution of 5 g/L heavy crude oil in heptol 1:1. The water contact angles on Surfaces IV and V were 27 ± 3° and 94 ± 3°. Top-view (a) and side-view images (b) of the receding oil droplet with time, t = 0 – 300 s. Time-dependency of the droplet contact points A, B, C and D (c) and the apparent droplet contact angle of Point D (d). In (c), 0 mm is the initial position of contact point A. Repeat measurements on the oil-contaminated surfaces showed

reasonable reproducibility for both the receding rates and steady-state apparent contact angles, see Fig. S2b of the Supporting Information.

Typical receding dynamics of a heavy crude oil droplet positioned equally at the wettability boundary of partially- and fully-oil-contaminated surfaces are shown in Fig. 6. With a more negative $\frac{\Delta G}{\Delta A}$ on Surface IV than Surface V, the heavy crude oil droplet preferentially moved towards Surface V. However, during droplet motion on Surface IV, the heavy crude oil droplet was seen to separate into several smaller daughter droplets that remained on Surface IV. This observation was found to be repeatable although slight variation was seen in the number and size of daughter droplets produced (Fig. S2b). With the number of daughter droplets determined from the top view images (Fig. 6a), it was the side view images that provided insight into how the daughter droplets were formed. The image at t = 17 s (Fig. 6b) showed a concave curvature near the droplet apex which can occur if there is resistance to directional motion.[29] This mechanism is explored further below using LBM simulations.

Due to the primary droplet separating into smaller daughter droplets, the droplet receding rates on Surfaces IV and V (Fig. 6c) could only be approximated using the edge-detection method. Consistent with the initial conditions (based on $\frac{\Delta G}{\Delta A}$ values), the receding velocity on Surface IV exceeded that of Surface V, with values shown in Fig. 6c inset. Within the measurement resolution, Point D stopped receding after 80 s and the apparent contact angle remained unchanged thereafter (Fig. 6d), while on Surface IV the contact point (A to B to C) receded for up to 150 s.
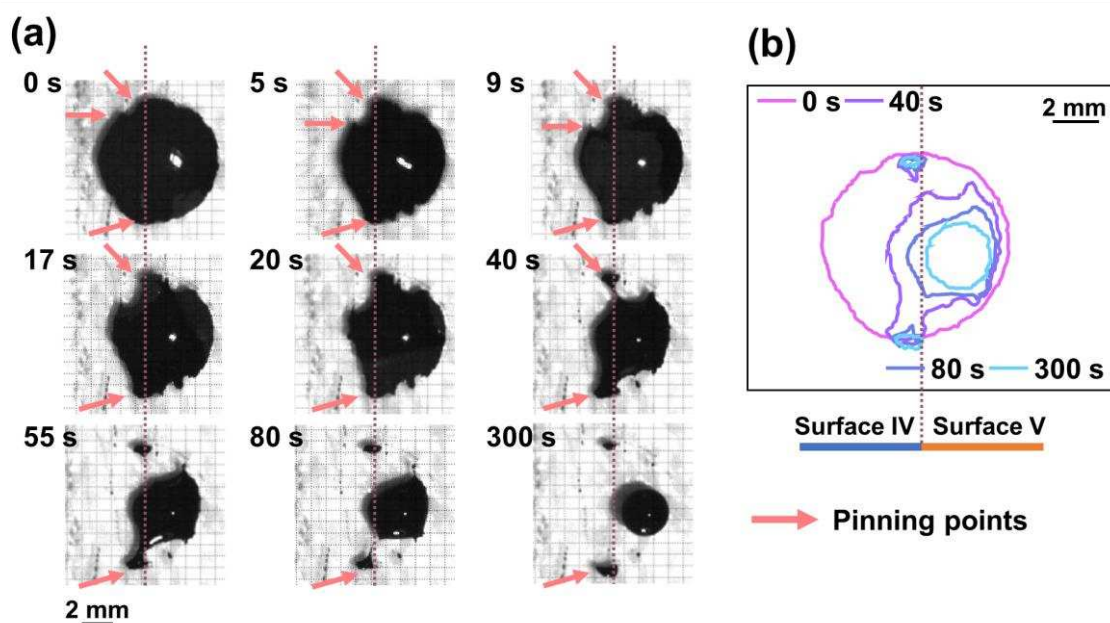
Figure 7. Top-view images showing the dynamic dewetting of a heavy crude oil droplet initially positioned centrally at the wettability boundary (a). The glass substrate was treated with a solution of 5 g/L heavy crude oil in heptol 1:1. The water contact angles on Surfaces IV and V were 27 ± 3° and 94 ± 3°. The arrows indicate regions of droplet pinning. Time-dependent contact line profiles of the receding heavy crude oil droplet (b).

Figure 7 highlights the non-uniformity of the heavy crude oil droplet dewetting process on partially- and fully-oil-contaminated surfaces. As the oil droplet recedes on both surfaces, the contact line on Surface IV is very irregular due to multiple points of apparent contact line pinning (relative to the bulk droplet dewetting rate). While there is some apparent contact line pinning on Surface V, it does not result in the formation of large (~1 mm) daughter droplets. Close to the wettability boundary on Surface IV there are at least two large daughter droplets that formed as the oil droplet recedes on the surface. Further analysis of the images (Fig. 7b) revealed those daughter droplets formed in a region where the contact line moved significantly slower (due to the apparent contact line pinning) than the contact line further away from the wettability boundary. Such differences in relative velocity of the moving contact lines leads to the formation of a liquid bridge that collapses to form a smaller daughter droplet. In the same experiment there are regions further away from the wettability boundary where the contact line appears to be pinned, but as the droplet continues to recede the contact line unpins before a daughter droplet is formed.

Surface characterization of Surface IV (Fig. 3) revealed a gradient boundary (diffuse) as the level of contamination decreased from fully-contaminated to no contamination. In this region the substrate wettability was heterogeneous and it is the heterogeneity that is thought to promote the disparity between the locally moving contact lines which causes the primary droplet to separate. When lowering the measurement temperature to 50°C the dewetting dynamics slowed slightly, however, daughter droplets were still formed, see Fig. S2b of the Supporting Information. Although there was variation in the receding rates (as determined by the apparent contact angle, Fig. S2b), such differences did not change the observed behavior. Only at 30°C were daughter droplets not observed, although the rate of droplet dewetting was negligible after 2000 s, hence insufficient dewetting occurred on the heterogeneous surface. This seems to suggest that the relative motion of the contact line on surfaces of varying wettability is crucial to form daughter droplets, with behavior strongly influenced by surface heterogeneity in the vicinity of the three-phase (triple) line, in good agreement with the theoretical scrutiny of a similar problem that was considered by Bormashenko.[48]

Furthermore, the influence of surface roughness on the dewetting behavior has been considered. Roughening the glass substrate using sandpaper (grit P2500) so that the R_q value is approximately equal to that of Surface V, it was found that the dewetted droplet did not separate on the unmodified surface but did form daughter droplets on the oil-contaminated surface (Fig. S7). Therefore, with behavior being consistent to that observed on the unroughened surfaces, the effect of roughness within the range relevant to the current study is thought to be negligible and thus not accounted for in the LBM simulations.
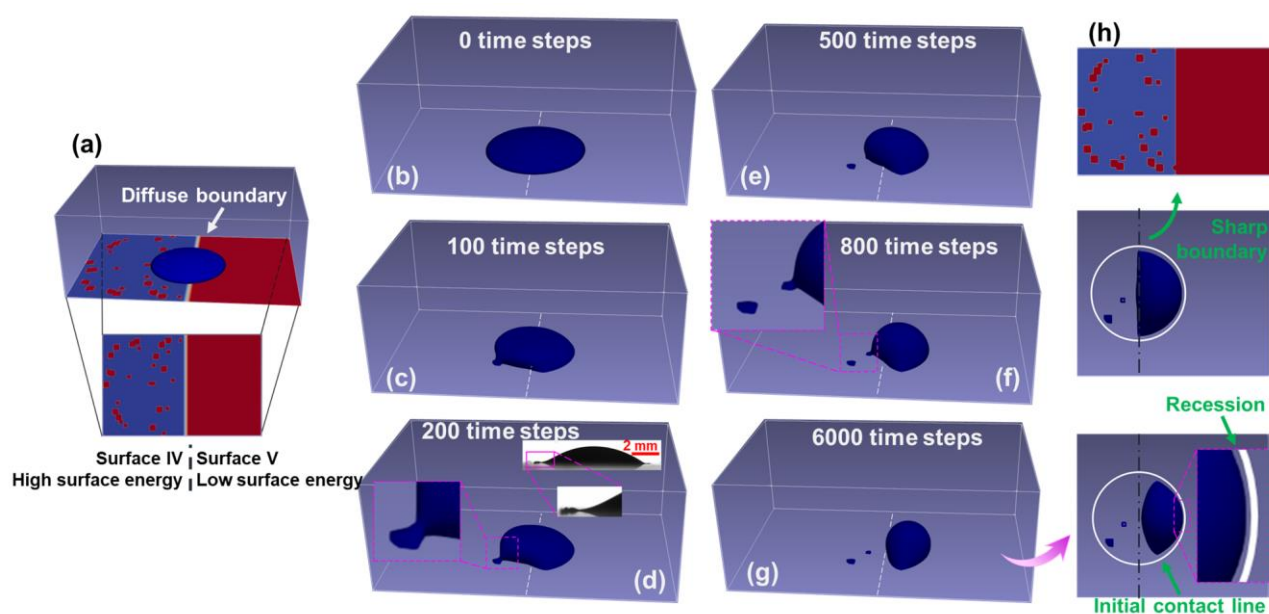

Figure 8. Simulated droplet dewetting using the Lattice Boltzmann method. To mimic the experiment, the substrate was formed using a higher surface energy substrate (blue color representing Surface IV), with advancing and receding contact angles through the continuous phase of 64° and 64°, and a lower surface energy substrate (red color representing Surface V), with advancing and receding contact angles of 81° and 175°, respectively (a). To account for the gradient boundary on Surface IV (Fig. 3), patches of Surface V were randomly positioned close to the wettability boundary. Moreover, the wettability boundary was modelled as a linear function diffuse boundary between the two surfaces. Snap-shots of the receding droplet are shown in (b) – (g) at increasing LBM time-steps. The steady-state condition is shown at 6000 time-steps. The steady-state of simulated droplet on a sharp wetting boundary is shown in (h) with other wetting properties same as (a).

To complement the experimental observations and explore further the role of localized contact-line pinning and relative movement of the oil-water interface in the formation of daughter droplets, the

LBM simulations were adapted to better reflect the characteristics of the oil-contaminated surfaces. This included: i) generating heterogeneous wettability on Surface IV by introducing patches of Surface V, to reflect surface heterogeneity beyond the wettability boundary, and ii) applying a diffuse rather than a sharp boundary to better reflect behavior at the wettability boundary. Note that on the basis of the negligible effects of roughness mentioned above, substrate roughness was not considered in the simulations.

For (i), Surface IV was imaged using AFM (Fig. 2d) and the bearing analysis method used to determine the fraction of the substrate contaminated by clustered macromolecules. The baseline for the bearing analysis method was taken to be the average height of the control surface (Fig. 2a). Based on the method, the surface fraction contaminated was 7.5% and this value was used in the LBM simulation to randomly distribute patches of Surface V on Surface IV, with the patch size either being 2 or 3 lattice units (note that the lattice size of the substrate is 141×55). For (ii), a diffuse boundary of width 15 lattice units was used to transition linearly from the θ_A and θ_R on Surface IV to the corresponding values on Surface V. Its inclusion is justified in the discussion below.

Without adjusting θ_R on Surface V (81°), no daughter droplets were generated when the droplet receded on Surface IV. Increasing θ_R to 175° on Surface V led to daughter droplets being formed on Surface IV and a straight contact line was observed at the wettability boundary when it was modelled as a sharp boundary (Fig. 8h). As indicated in Fig. 3, the wettability transition is more diffuse, and accounting for this was important in capturing the correct dynamics and final droplet footprint observed experimentally. The size of the diffuse boundary was scaled based on the length of the gradient boundary (Fig. 3b) to the droplet spread length in air. Inclusion of the diffuse boundary led to a curved contact line beyond the wettability boundary and the steady-state shape of the receded droplet qualitatively matched the experiment (Fig. 8g). The diffuse boundary promoted the droplet to recede onto Surface V due to the Cassie effect,[14] with the contact line adjusting to the average wettability of the heterogeneous substrate, i.e. $\cos\theta = \sum f_i \cos\theta_i$, where f_i and θ_i are the fractional surface area and local contact angle of component i, respectively.

By slightly decreasing θ_R on Surface V to 164°, non-uniform dewetting was observed again but no daughter droplets were formed (Fig. S5a), thus confirming the existence of a critical θ_R for daughter droplet formation, an understanding that could not be verified experimentally. Since θ_R correlates to the droplet-substrate adhesion, and adhesion affects the rate of motion of the contact line,[49] when

lowering θ_R on Surface V, the difference in mobility of the two contact lines on Surface IV and patches of Surface V is less, thus the potential for a liquid neck to form and then collapse is lowered. However, since rate is a time-dependent property, the critical θ_R will be a function of the patch size. Such insight could be explored using the LBM simulation, and when doubling or halving the patch size the critical θ_R was 162° (Fig. S5b) and 169° (Fig. S5c), respectively. Such findings are reasonable since larger patches extend the time of differing relative motions, which promotes the formation of a liquid neck that can eventually result in daughter droplets being formed if the liquid neck is significantly elongated (reducing thickness of the liquid film which becomes unstable and collapses). With the physical behaviors agreeing with those observed experimentally, the LBM simulation has provided a crucial level of insight regarding the surface properties that govern daughter droplet formation, specifically the critical θ_R that also depends on the heterogenous patch size. The LBM simulation has also given confidence to the proposed mechanism by which daughter droplets are formed.

5. Conclusions

Migrating droplets on surfaces are ubiquitously encountered, hence there remains great scientific interest to understand droplet-surface interactions, to then be able to tune those interactions for a particular response.[50,51] While droplet dynamics have been fundamentally understood by studying droplets on model surfaces (i.e. pillared, pored and simulated),[26,52,53] few studies have considered more 'realistic' surfaces where chemical and surface heterogeneity coexist. Furthermore, droplet dewetting is often considered by applying an external force (i.e. droplet dragging, reducing the droplet volume, droplet migration in an electric field),[54–57] with little insight into the dynamics of droplet dewetting when the droplet volume is conserved. The spontaneous dewetting of highly viscous oil droplets on surfaces prepared by irregular chemical deposition and then simulated using 3D-LBM, has shown the critical importance of surface heterogeneity (hydrophobic patch size and θ_R) on the potential to form small daughter droplets during dewetting.

The dewetting dynamics of highly viscous oil droplets across a wettability boundary were compared on surfaces modified with i) methyloctyldichlorosilane and ii) clustered macromolecules. For methyloctyldichlorosilane, a sharp wettability boundary was formed between Surfaces II and III, and when the oil droplet was positioned at the boundary and subsequently immersed in water, the droplet uniformly receded to the hydrophobic surface (Surface III), as expected. The final droplet shape was a distorted spherical cap with a straight contact line at the wettability boundary, since the droplet could not recede on Surface III. The 3D-LBM simulation revealed that high θ_A (140°) and θ_R (175°) on

Surface III were needed to qualitatively describe the overall dynamics of the receding oil droplet. For clustered macromolecules, the transition between the two surface wettabilities was characterized by a region of surface heterogeneity, where hydrophobic patches were randomly dispersed on the hydrophilic surface. When the oil droplet dewetted, the mobility of the receding contact line was uneven and led to the formation of small daughter droplets. The 3D-LBM simulation revealed that the discontinuous dewetting resulted from differences in the local contact line migration relative to the bulk droplet, with this parameter strongly dependent on the θ_R and hydrophobic patch size, with the latter influencing the critical θ_R to form daughter droplets.

The current study reveals the importance of local variations on the surface to the overall dynamics of a dewetting droplet. While surface variations were considered from the perspective of differing surface energies, as supported by the 3D-LBM simulations, the role of surface roughness is yet to be fully determined. While surface roughness does not directly change the surface energy, it does change the droplet-surface contact area, which can influence the apparent mobility of the contact line, a property that in the current study has been shown to affect the formation of daughter droplets. Further work in this area will lead to a much greater understanding of droplet dynamics on surfaces where both variable structural and chemical heterogeneity coexist.

Supplementary Information

S1. Surface preparation methods; S2. Heavy crude oil droplet dewetting dynamics at different temperature; S3. Droplet dewetting – dimensionless numbers and spreading parameters; S4. FTIR characterization of the oil-contaminated surface; S5. LBM simulation: Wettability boundary and no surface heterogeneity; S6. LBM simulation: Wettability boundary and surface heterogeneity. S7. Heavy crude oil droplet dewetting dynamics on roughened surfaces.

Acknowledgements

References

(1)   Chakraborty, M.; Ghosh, U. U.; Chakraborty, S.; Dasgupta, S. Thermally Enhanced Self-Propelled Droplet Motion on Gradient Surfaces. *RSC Adv.* **2015**, *5* (56), 45266–45275. https://doi.org/10.1039/c5ra00469a.

(2)   Basu, S.; Nandakumar, K.; Masliyah, J. H. A Visual Study of High Grade Oil Sand Disintegration Process. *J. Colloid Interface Sci.* **1998**, *205* (1), 201–203. https://doi.org/10.1006/jcis.1998.5565.

(3)   Al-Milaji, K. N.; Radhakrishnan, V.; Kamerkar, P.; Zhao, H. PH-Modulated Self-Assembly of Colloidal Nanoparticles in a Dual-Droplet Inkjet Printing Process. *J. Colloid Interface Sci.* **2018**, *529*, 234–242. https://doi.org/10.1016/j.jcis.2018.06.008.

(4)   Akai, T.; Blunt, M. J.; Bijeljic, B. Pore-Scale Numerical Simulation of Low Salinity Water Flooding Using the Lattice Boltzmann Method. *J. Colloid Interface Sci.* **2020**, *566*, 444–453. https://doi.org/10.1016/j.jcis.2020.01.065.

(5)   Huang, D. J.; Leu, T. S. Fabrication of High Wettability Gradient on Copper Substrate. *Appl. Surf. Sci.* **2013**, *280*, 25–32. https://doi.org/10.1016/j.apsusc.2013.04.065.

(6)   Tadmor, R.; Baksi, A.; Gulec, S.; Jadhav, S.; N, H. E.; Somasi, V.; Tadmor, M.; Tang, S.; Wasnik, P.; Yadav, S. Defying Gravity : Drops That Climb up a Vertical Wall of Their Own Accord. *J. Colloid Interface Sci.* **2020**, *562*, 608–613. https://doi.org/10.1016/j.jcis.2019.10.120.

(7)   Chaudhury, M. K.; Whitesides, G. M. How to Make Water Run Uphill. *Science* **1992**, 256 (5063), 1539-1541. https://doi.org/10.1126/science.256.5063.1539.

(8)   Banuprasad, T. N.; Vinay, T. V.; Subash, C. K.; Varghese, S.; George, S. D.; Varanakkottu, S. N. Fast Transport of Water Droplets over a Thermo-Switchable Surface Using Rewritable Wettability Gradient. *ACS Appl. Mater. Interfaces* **2017**, *9* (33), 28046–28054. https://doi.org/10.1021/acsami.7b07451.

(9)   Ju, J.; Xiao, K.; Yao, X.; Bai, H.; Jiang, L. Bioinspired Conical Copper Wire with Gradient Wettability for Continuous and Efficient Fog Collection. *Adv. Mater.* **2013**, *25* (41), 5937–5942. https://doi.org/10.1002/adma.201301876.

(10)   Hu, R.; Wang, N.; Hou, L.; Cui, Z.; Liu, J.; Li, D.; Li, Q.; Zhang, H.; Zhao, Y. A Bioinspired Hybrid Membrane with Wettability and Topology Anisotropy for Highly Efficient Fog Collection. *J. Mater. Chem. A* **2019**, 7, 124–132. https://doi.org/10.1039/c8ta10615k.

(11)   Ju, J.; Zheng, Y.; Jiang, L. Bioinspired One-Dimensional Materials for Directional Liquid Transport. *Acc. Chem. Res.* **2014**, *47* (8), 2342–2352. https://doi.org/10.1021/ar5000693.

(12)   Lv, F.; Zhao, F.; Cheng, D.; Dong, Z.; Jia, H.; Xiao, X; Orejon, D. Bioinspired Functional SLIPSs and Wettability Gradient Surfaces and Their Synergistic Cooperation and Opportunities for Enhanced Condensate and Fluid Transport. *Adv. Colloid Interface Sci.* **2022**, *299*, 102564. https://doi.org/10.1016/j.cis.2021.102564.

(13)   Zheng, Y.; Bai, H.; Huang, Z.; Tian, X.; Nie, F.; Zhao, Y.; Zhai, J.; Jiang, L. Directional Water Collection on Wetted Spider Silk. *Nature* **2010**, *463*, 2–5. https://doi.org/10.1038/nature08729.

(14)   Carmeliet, J.; Chen, L.; Kang, Q.; Derome, D. Beyond-Cassie Mode of Wetting and Local Contact Angles of Droplets on Checkboard-Patterned Surfaces. *Langmuir* **2017**, *33* (24), 6192–6200. https://doi.org/10.1021/acs.langmuir.7b01471.

(15)   Wu, Y.; Kuzina, M.; Wang, F.; Reischl, M.; Selzer, M.; Nestler, B.; Levkin, P. A. Equilibrium Droplet Shapes on Chemically Patterned Surfaces: Theoretical Calculation, Phase-Field Simulation, and Experiments. *J. Colloid Interface Sci.* **2022**, *606*, 1077–1086. https://doi.org/10.1016/j.jcis.2021.08.029.

(16)   Huang, Z. New Equations of Wetting. *Philos. Mag. Lett.* **2020**, *100* (4), 181–188. https://doi.org/10.1080/09500839.2020.1740811.

(17)   Yildirim Erbil, H. Dependency of Contact Angles on Three-Phase Contact Line: A Review. *Colloids and Interfaces* **2021**, *5* (1). https://doi.org/10.3390/colloids5010008.

(18) Joanny, J. F.; De Gennes, P. G. A Model for Contact Angle Hysteresis. *J. Chem. Phys.* **1984**, *81* (1), 552–562. https://doi.org/10.1063/1.447337.

(19) Chang, B.; Oskari, K.; Pini, L.; Levkin A. P.; Ras, R. H. A.; Zhou Q. Nanoliter Deposition on Star-Shaped Hydrophilic– Superhydrophobic Patterned Surfaces. *Soft Matter* **2018**, *14*, 7500–7506. https://doi.org/10.1039/c8sm01288a.

(20) Orejon, D.; Sefiane, K.; Shanahan, M. E. R. Stick-Slip of Evaporating Droplets: Substrate Hydrophobicity and Nanoparticle Concentration. *Langmuir* **2011**, *27* (21), 12834–12843. https://doi.org/10.1021/la2026736.

(21) Tian, D.; Zhang, N.; Zheng, X.; Hou, G.; Tian, Y.; Du, Y.; Jiang, L.; Dou, S. X. Fast Responsive and Controllable Liquid Transport on a Magnetic Fluid/Nanoarray Composite Interface. *ACS Nano* **2016**, *10* (6), 6220–6226. https://doi.org/10.1021/acsnano.6b02318.

(22) Gauthier, A.; Rivetti, M.; Teisseire, J.; Barthel, E. Role of Kinks in the Dynamics of Contact Lines Receding on Superhydrophobic Surfaces. *Phys. Rev. Lett.* **2013**, *110* (4), 1–5. https://doi.org/10.1103/PhysRevLett.110.046101.

(23) Jiang, Y.; Choi, C. H. Droplet Retention on Superhydrophobic Surfaces: A Critical Review. *Adv. Mater. Interfaces* **2021**, *8* (2). https://doi.org/10.1002/admi.202001205.

(24) Shanahan, M. E. R. Simple Theory of "Stick-Slip" Wetting Hysteresis. *Langmuir* **1995**, *11* (3), 1041–1043. https://doi.org/10.1021/la00003a057.

(25) Moffat, J. R.; Sefiane, K.; Shanahan, M. E. R. Effect of TiO2 Nanoparticles on Contact Line Stick-Slip Behavior of Volatile Drops. *J. Phys. Chem. B* **2009**, *113* (26), 8860–8866. https://doi.org/10.1021/jp902062z.

(26) Jiang, Y.; Xu, W.; Sarshar, M. A.; Choi, C. H. Generalized Models for Advancing and Receding Contact Angles of Fakir Droplets on Pillared and Pored Surfaces. *J. Colloid Interface Sci.* **2019**, *552*, 359–371. https://doi.org/10.1016/j.jcis.2019.05.053.

(27) Basu, S.; Nandakumar, K.; Lawrence, S.; Masliyah, J. Effect of Calcium Ion and Montmorillonite Clay on Bitumen Displacement by Water on a Glass Surface. *Fuel* **2004**, *83* (1), 17–22. https://doi.org/10.1016/S0016-2361(03)00222-9.

(28) Basu, S.; Nandakumar, K.; Lawrence, S.; Masliyah, J. Effect of Hydrophobic and Hydrophilic Clays on Bitumen Displacement by Water on a Glass Surface. *Ind. Eng. Chem. Res.* **1998**, *37* (3), 959–965. https://doi.org/10.1021/ie9705012.

(29) Basu, S.; Nandakumar, K.; Masliyah, J. H. Study on Daughter Droplets Formation in Bitumen/Glass/Water Contact Line Displacement Due to Instability. *Fuel* **2000**, *79* (7), 837–841. https://doi.org/10.1016/S0016-2361(99)00203-3.

(30) Redon, C.; Brocharrd-Wyart, F.; Rondelez, F. Dynamics of Dewetting. *Phys. Rev. Lett.* **1991**, *66* (6). https://doi.org/10.1103/PhysRevLett.66.715.

(31) Tangparitkul, S.; Charpentier, T.; Pradilla, D.; Harbottle, D. Interfacial and Colloidal Forces Governing Oil Droplet Displacement: Implications for Enhanced Oil Recovery. *Colloids and Interfaces* **2018**, *2* (3), 30. https://doi.org/10.3390/colloids2030030.

(32) Xie, C.; Lei, W.; Balhoff, M. T.; Wang, M.; Chen, S. Self-Adaptive Preferential Flow Control Using Displacing Fluid with Dispersed Polymers in Heterogeneous Porous Media. *J. Fluid Mech.* **2021**, *906*, A10. https://doi.org/10.1017/jfm.2020.763.

(33) Zu, Y. Q.; Yan, Y. Y. Lattice Boltzmann Method for Modelling Droplets on Chemically Heterogeneous and Microstructured Surfaces with Large Liquid-Gas Density Ratio. *IMA J. Appl. Math.* **2011**, *76* (5), 743–760. https://doi.org/10.1093/imamat/hxr047.

(34) Jackson, F. F.; Kubiak, K. J.; Wilson, M. C. T.; Molinari, M.; Stetsyuk, V. Droplet Misalignment Limit for Inkjet Printing into Cavities on Textured Surfaces. *Langmuir* **2019**, *35* (29), 9564–9571. https://doi.org/10.1021/acs.langmuir.9b00649.

(35) Al-Ghaithi, K. H. A.; Harlen, O. G.; Kapur, N.; Wilson, M. C. T. Morphologies and Dynamics of Micro-Droplet Impact onto an Idealised Scratch. *J. Fluid Mech.* **2021**, *925*, 1–34. https://doi.org/10.1017/jfm.2021.638.

(36)   Sudhakar, T.; Das, A. K. Evolution of Multiphase Lattice Boltzmann Method: A Review. *J. Inst. Eng. Ser. C* **2020**, *101* (4), 711–719. https://doi.org/10.1007/s40032-020-00600-8.

(37)   Krüger, T.; Kusumaatmaja, H.; Kuzmin, A.; Shardt, O.; Silva, G.; Viggen, E. M. *The Lattice Boltzmann Method*; Springer, **2017**. https://doi.org/10.1007/978-3-319-44649-3.

(38)   Shan, X.; Chen, H. Simulation of Nonideal Gases and Liquid-Gas Phase Transitions by the Lattice Boltzmann Equation. *Physical Review E*, **1994**, *49* (4), 2941–2948. https://doi.org/10.1103/PhysRevE.49.2941.

(39)   Shan, X.; Chen, H. Lattice Boltzmann Model for Simulating Flows with Multi Phases and Components. *Physical Review E*, **1993**, *47* (3), 1815–1819. https://doi.org/10.1103/PhysRevE.47.1815.

(40)   Yuan, P.; Schaefer, L. Equations of State in a Lattice Boltzmann Model. *Phys. Fluids* **2006**, *18* (4). https://doi.org/10.1063/1.2187070.

(41)   Hu, A.; Li, L.; Chen, S.; Liao, Q.; Zeng, J. On Equations of State in Pseudo-Potential Multiphase Lattice Boltzmann Model with Large Density Ratio. *Int. J. Heat Mass Transf.* **2013**, *67*, 159–163. https://doi.org/10.1016/j.ijheatmasstransfer.2013.08.005.

(42)   Li, Q.; Luo, K. H.; Li, X. J. Lattice Boltzmann Modeling of Multiphase Flows at Large Density Ratio with an Improved Pseudopotential Model. *Phys. Rev. E - Stat. Nonlinear, Soft Matter Phys.* **2013**, *87* (5). https://doi.org/10.1103/PhysRevE.87.053301.

(43)   Ding, H.; Spelt, P. D. M. Wetting Condition in Diffuse Interface Simulations of Contact Line Motion. *Phys. Rev. E - Stat. Nonlinear, Soft Matter Phys.* **2007**, *75* (4), 1–8. https://doi.org/10.1103/PhysRevE.75.046708.

(44)   Aissaoui, N.; Bergaoui, L.; Landoulsi, J.; Lambert, J. F.; Boujday, S. Silane Layers on Silicon Surfaces: Mechanism of Interaction, Stability, and Influence on Protein Adsorption. *Langmuir* **2012**, *28* (1), 656–665. https://doi.org/10.1021/la2036778.

(45)   Tangparitkul, S.; Hodges, C. S.; Ballard, D. A.; Niu, Z.; Pradilla, D.; Charpentier, T. V. J.; Xu, Z.; Harbottle, D. Dewetting Dynamics of Heavy Crude Oil Droplet in Low-Salinity Fluids at Elevated Pressures and Temperatures. *J. Colloid Interface Sci.* **2021**, *596*, 420–430. https://doi.org/10.1016/j.jcis.2021.03.130.

(46)   Lin, F.; He, L.; Primkulov, B.; Xu, Z. Dewetting Dynamics of a Solid Microsphere by Emulsion Drops. *J. Phys. Chem. C* **2014**, *118* (25), 13552–13562. https://doi.org/10.1021/jp412662x.

(47)   Masliyah, J. H.; Czarnecki, J.; Xu, Z. *Handbook on Theory and Practice of Bitumen Recovery from Athabasca Oil Sands Volume I: Theoretical Basis*; Kingsley, **2011**; Vol. 1. https://doi.org/10.7939/r3-nr43-8t34.

(48)   Bormashenko, E. A Variational Approach to Wetting of Composite Surfaces: Is Wetting of Composite Surfaces a One-Dimensional or Two-Dimensional Phenomenon? *Langmuir* **2009**, *25* (18), 10451–10454. https://doi.org/10.1021/la902458t.

(49)   Schmidt, D. L.; Brady, R. F.; Lam, K.; Schmidt, D. C.; Chaudhury, M. K. Contact Angle Hysteresis, Adhesion, and Marine Biofouling. *Langmuir* **2004**, *20* (7), 2830–2836. https://doi.org/10.1021/la035385o.

(50)   Pei, J.; Liao, Y.; Li, Q.; Shi, K.; Fu, J.; Hu, X.; Huang, Z.; Xue, L.; Xiao, X.; Liu, K. Single-Layer Graphene Prevents Cassie-Wetting Failure of Structured Hydrophobic Surface for Efficient Condensation. *J. Colloid Interface Sci.* **2022**, *615*, 302–308. https://doi.org/10.1016/j.jcis.2022.01.157.

(51)   Drelich, J. W. Contact Angles: From Past Mistakes to New Developments through Liquid-Solid Adhesion Measurements. *Adv. Colloid Interface Sci.* **2019**, *267*, 1–14. https://doi.org/10.1016/j.cis.2019.02.002.

(52)   Sarshar, M. A.; Jiang, Y.; Xu, W.; Choi, C. H. Depinning Force of a Receding Droplet on Pillared Superhydrophobic Surfaces: Analytical Models. *J. Colloid Interface Sci.* **2019**, *543*, 122–129. https://doi.org/10.1016/j.jcis.2019.02.042.

(53)   Yin, B.; Xie, X.; Xu, S.; Jia, H.; Yang, S.; Dong, F. Effect of Pillared Surfaces with Different

Shape Parameters on Droplet Wettability via Lattice Boltzmann Method. *Colloids Surfaces A Physicochem. Eng. Asp.* **2021**, *615*, 126259. https://doi.org/10.1016/j.colsurfa.2021.126259.

(54) Liu, T. L.; Chen, Z.; Kim, C. J. A Dynamic Cassie-Baxter Model. *Soft Matter* **2015**, *11* (8), 1589–1596. https://doi.org/10.1039/c4sm02651a.

(55) Dufour, R.; Brunet, P.; Harnois, M.; Boukherroub, R.; Thomy, V.; Senez, V. Zipping Effect on Omniphobic Surfaces for Controlled Deposition of Minute Amounts of Fluid or Colloids. *Small* **2012**, *8* (8), 1229–1236. https://doi.org/10.1002/smll.201101895.

(56) Xu, W.; Choi, C. H. From Sticky to Slippery Droplets: Dynamics of Contact Line Depinning on Superhydrophobic Surfaces. *Phys. Rev. Lett.* **2012**, *109* (2), 1–5. https://doi.org/10.1103/PhysRevLett.109.024504.

(57) Geng, H.; Feng, J.; Stabryla, L. M.; Cho, S. K. Dielectrowetting Manipulation for Digital Microfluidics: Creating, Transporting, Splitting, and Merging of Droplets. *Lab Chip* **2017**, *17* (6), 1060–1068. https://doi.org/10.1039/c7lc00006e.